

The Bright Supernova 1996cr in the Circinus Galaxy Imaged with VLBI: Shell Structure with Complex Evolution

Michael F. Bietenholz^{1,2}, Norbert Bartel¹, Franz E. Bauer^{3,4,5}, Vikram V. Dwarkadas⁶, Leon Mtshweni⁷, Carlos Orquera-Rojas^{3,4}, Simon Ellingsen⁸, Shinji Horiuchi⁹, and Anastasios Tzioumis¹⁰

¹*Department of Physics and Astronomy, York University, Toronto, M3J 1P3, Ontario, Canada*

²*SARAO/Hartebeesthoek Radio Astronomy Observatory, PO Box 443, Krugersdorp, 1740, South Africa*

³*Facultad de Física, Instituto de Astrofísica and Centro de Astroingeniería, Pontificia Universidad Católica de Chile, Casilla 306, Santiago 22, Chile*

⁴*Millennium Institute of Astrophysics (MAS), Nuncio Monseñor Sótero Sanz 100, Providencia, Santiago, Chile*

⁵*Space Science Institute, 4750 Walnut Street, Suite 205, Boulder, CO 80301, USA*

⁶*Department of Astronomy and Astrophysics, University of Chicago, 5640 S Ellis Avenue, Chicago, IL 60637, USA*

⁷*Department of Physics, University of Pretoria, Hatfield, Pretoria, 0028, South Africa*

⁸*School of Natural Sciences, University of Tasmania, Private Bag 37, Hobart, TAS 7001, Australia*

⁹*CSIRO Space & Astronomy, Canberra Deep Space Communications Complex, PO Box 1035, Tuggeranong, ACT 2901, Australia*

¹⁰*Australia Telescope National Facility, CSIRO, PO Box 76, Epping, NSW 1710, Australia*

Accepted for publication in MNRAS

ABSTRACT

We present broadband radio flux-density measurements supernova (SN) 1996cr, made with MeerKAT, ATCA and ALMA, and images made from very long baseline interferometry (VLBI) observations with the Australian Long Baseline Array. The spectral energy distribution of SN 1996cr in 2020, at age, $t \sim 8700$ d, is a power-law, with flux density, $S \propto \nu^{-0.588 \pm 0.011}$ between 1 and 34 GHz, but may steepen at > 35 GHz. The spectrum has flattened since $t = 5370$ d (2010). Also since $t = 5370$ d, the flux density has declined rapidly, with $S_{9\text{ GHz}} \propto t^{-2.9}$. The VLBI image at $t = 8859$ d shows an approximately circular structure, with a central minimum reminiscent of an optically-thin spherical shell of emission. For a distance of 3.7 Mpc, the average outer radius of the radio emission at $t = 8859$ d was $(5.1 \pm 0.3) \times 10^{17}$ cm, and SN 1996cr has been expanding with a velocity of 4650 ± 1060 km s⁻¹ between $t = 4307$ and 8859 d. It must have undergone considerable deceleration before $t = 4307$ d. Deviations from a circular shell structure in the image suggest a range of velocities up to ~ 7000 km s⁻¹, and hint at the presence of a ring- or equatorial-belt-like structure rather than a complete spherical shell.

Key words: Supernovae: individual (SN 1996cr) – radio continuum: general

1 INTRODUCTION

Supernova (SN) 1996cr, in the nearby Circinus Galaxy had the highest radio flux density ever observed for optically-identified radio supernova (163 mJy at 8.3 GHz; Bauer 2007; Bauer et al. 2008), as well as being one of only a handful of supernovae which can still be observed in radio more than 20 yr after the explosion. It was seen in 2001 in X-rays (Samburina et al. 2001), and subsequently identified as a possible SN (Bauer et al. 2001), but only firmly identified as a SN in 2008 (Bauer et al. 2008). It was not identified till well after the explosion, so the explosion date, t_0 , is not accurately known. We take $t_0 = 1995$ Sep. 7 (MJD = 49968), which is the midpoint of the range given in Bauer et al. (2008), and all our times, t , are with respect to this t_0 . We take the Circinus

Galaxy and SN 1996cr to be at a distance $D \sim 3.7$ Mpc,¹ and we indicate the dependence of our derived quantities on D , which is only known to about 25% accuracy.

SN 1996cr was classified as a Type IIn supernova in 2007,

¹ We average the distance derived from the redshift using the NASA/IPAC Extragalactic Database (NED; <https://ned.ipac.caltech.edu>), after correction for infall to Virgo, the Great Attractor and Shapley supercluster and use $H_0 = 67.4$ km s⁻¹ Mpc⁻¹ (Planck Collaboration et al. 2020), which distance is 3.16 ± 0.22 Mpc, and the redshift-independent value listed on NED of 4.2 Mpc to arrive at 3.7 Mpc. However we note that there is some disagreement on the distance to Circinus, see discussion in Mondal et al. (2021), with values as high as 4.2 Mpc (e.g. Freeman et al. 1977) and as low as 2.6 Mpc (Rózańska et al. 2018) being used in the literature.

around a decade after the explosion (Bauer et al. 2008; see also Ransome et al. 2021), but there are no observations constraining its type at early times.² Type IIn supernovae are characterized by relatively narrow H features superimposed on the broader emission lines, and are associated with strong interaction with a dense circumstellar medium (CSM; e.g. Fransson et al. 2014; Smith 2014) produced by winds and outflows from the progenitors before the explosions. Type IIn SNe (for example SN 1986J and SN 1988Z) tend to exhibit stronger and longer-lasting radio emission than other Types of SNe (Bietenholz et al. 2021b), as well as often having stronger X-ray emission at late times (e.g. Dwarkadas & Gruszko 2012).

SN 1996cr has remained unusually bright in both radio and X-rays for more than two decades, and is one of only a small number of long-lived core-collapse SNe (CCSNe) whose evolution can be studied over more than a decade. Its close distance of 3.7 Mpc makes it easier to observe than most other Type II SNe. SN 1996cr showed a rapid rise in radio emission around 1 yr after the explosion and then a plateau lasting for several more years (Bauer et al. 2008; Meunier et al. 2013). The X-rays showed a more gradual increase lasting till ~ 10 yr after the explosion (Quirola-Vásquez et al. 2019).

SN 1996cr’s rise in radio and X-rays is attributed to the SN shock interacting with a dense region of CSM (Bauer et al. 2008; Dwarkadas et al. 2010). SN 1996cr first exploded in a lower-density region, but then 1 \sim 2 yr after the explosion, the forward shock interacted with a region of dense CSM, which is characterized by Bauer et al. (2008) and Dwarkadas et al. (2010) as a shell formed during an episode of mass-loss from the progenitor. The inner radius of the dense CSM has been taken to be $\sim 10^{17}$ cm based largely on modelling of the emission at various wavebands (Dwarkadas et al. 2010; Dewey et al. 2011; Quirola-Vásquez et al. 2019) and constrained by the first VLBI measurement (Bauer et al. 2008). The dense CSM was likely formed by the interaction of the slow but dense red supergiant (RSG) wind with the fast, low-density, Wolf-Rayet (W-R) or blue supergiant (BSG) wind starting some 10^3 to 10^4 yr before the explosion. Even when starting with spherically symmetric winds, factors such as the magnetic field, turbulence within the bubble, presence of a binary companion, and hydrodynamic, magneto-hydrodynamic and ionization front instabilities (see Dwarkadas 2022, and references therein), can all lead to significant departures from sphericity. These can be exacerbated by the presence of an asymmetric surrounding medium, giving rise to a complex morphology.

2 TOTAL FLUX DENSITY OBSERVATIONS WITH MEERKAT, ATCA AND ALMA

2.1 MeerKAT Observations

We observed SN 1996cr with MeerKAT³ on 2018 May 4 (proposal code SCI-20180222-MB-01; we give the midpoint

² Some SNe, e.g. SN 2014C (Milisavljevic et al. 2015), initially show normal Type II spectra, and only after some time evolve to reveal IIn characteristics.

³ Operated by the South African Radio Astronomy Observatory (SARAO).

dates) and also used archival MeerKAT observations from 2018 July 20 (code SSV-20180428-FC-01), both at a central frequency of 1.28 GHz with a bandwidth of 856 MHz split into 4096 channels. The data were reduced using a combination of the OxKAT scripts (Heywood 2020) and manual reduction using the Common Astronomy Software Applications package (CASA; CASA Team et al. 2022). To determine the flux density of the SN on the scale of Stevens-Reynolds 2016 (Partridge et al. 2016), as well as to calibrate the instrumental bandpass, we observed the sources PKS J1939–6342 and PKS J0408–6544 (QSO B0408–65) on 2004 May 4, and 3C 286 on 2018 July 20. For phase and amplitude calibration, we used the sources PKS J1424–4913 and PKS J1619–8418. The data were self-calibrated in phase, but not amplitude.

The entire primary-beam area was imaged, and SN 1996cr and the Circinus Active Galactic Nucleus (AGN), as well as unrelated background sources were deconvolved using the CLEAN algorithm (CASA:tclean). SN 1996cr is well separated from the AGN of the Circinus Galaxy. We estimated the flux densities by fitting a model consisting of an unresolved source⁴ and a baseline- or zero-level to a small region of the image around SN 1996cr, with the former being interpreted as the SN, and the latter as the diffuse emission from the galaxy. Although this estimate of the diffuse emission is approximate, its value was smaller than our stated uncertainties, so its presence does not significantly impact our flux density determination for SN 1996cr. For the 2018 July 20 observation with the full MeerKAT, the resolution was $\sim 5''$, SN 1996cr was 99 mJy, the image background rms level was $19 \mu\text{Jy beam}^{-1}$, and the fitted zero level was 2% of the peak brightness of SN 1996cr. For the 2018 May 4 observation, for which only 16 dishes were used, the corresponding values were $8''$, 107 mJy, $98 \mu\text{Jy beam}^{-1}$, and $\sim 5\%$ of the SN 1996cr peak. As well as the statistical uncertainty, our flux density uncertainties include, and are dominated by, a 10% systematic uncertainty due to the flux-density bootstrapping (see, e.g. Driessen et al. 2022). All flux density determinations are listed in Table 1.

2.2 ATCA Observations

We observed SN 1996cr in 2020 with the Australia Telescope Compact Array (ATCA; Project Code C3323). The observations were reduced using CASA. We again used the flux-density scale of Stevens-Reynolds 2016 (Partridge et al. 2016), and set the scale using observations of PKS J1939–6342. (Partridge et al. 2016). The data were self-calibrated in phase, but not amplitude, and images deconvolved using the CLEAN algorithm (CASA:tclean). The FWHM resolution ranged from $2.8''$ at 2.1 GHz to $0.3''$ at 34 GHz. The flux densities were measured from the resulting CLEAN images in the same way as described above for MeerKAT, and our uncertainties include a 5% uncertainty in the flux-density bootstrapping. The systematic uncertainty is the dominant contribution to the uncertainty in the flux density of SN 1996cr at all frequencies except 9 GHz. The values are listed in Table 1.

⁴ An unresolved source in the images is an elliptical Gaussian with the dimensions and orientation fixed to those of the restoring beam.

2.3 ALMA Observations

We observed SN 1996cr also with the Atacama Large Millimeter Array on several occasions in 2019, as part of program #2018.1.00007.S (PI: F. Bauer) at 108.0, 223.0, 339.9, and 465.5 GHz (bands 3, 6, 7, and 8, respectively) on the dates given in Table 1 below. The observations were taken with the Atacama Compact Array of ALMA (ACA), and centred on the SN position, with a total bandwidth of 7.5 GHz in each frequency. The data were reduced using CASA. The flux density scale at ALMA is set by observations of one of a set of unresolved calibrator sources (“grid” sources), referred ultimately to solar system objects, and is accurate to $\sim 10\%$ (Francis et al. 2020). Spectral cubes were inspected by eye to flag and remove any channels affected by strong line emission (e.g. CO) associated with the disk of host galaxy. Images were again made using the CLEAN algorithm (CASA:tclean), adopting Briggs weighting with `robust` = 0.

At 108 GHz, the resolution of the ACA is $12''$, and SN 1996cr and the Circinus nucleus are ~ 2 beamwidths apart, and have some degree of overlapping emission. There is also the possibility of some diffuse emission from the galaxy at the location of SN 1996cr. To allow for these two factors, we determined the flux density of SN 1996cr by fitting models to the region of the image near SN 1996cr. We used three models: 1) an unresolved source for SN 1996cr with a constant background level, 2) an unresolved source for SN 1996cr, with a background level and slope, and 3) using a larger fitting area, an unresolved source for SN 1996cr and an elliptical Gaussian for the nucleus of the Circinus galaxy. We adopt the mean over the three different models as the final flux density of SN 1996cr, and the standard deviation over the three models as an estimate of the uncertainty in separating SN 1996cr from the background, to obtain a flux density of $4320 \pm 1120 \mu\text{Jy}$ for SN 1996cr. (The galaxy contribution at SN 1996cr’s location was smaller than the uncertainty at $\sim 400 \mu\text{Jy beam}^{-1}$). The image rms was $300 \mu\text{Jy beam}^{-1}$, and we take 10% for the flux calibration uncertainty to arrive at a final value of $4320 \pm 1230 \mu\text{Jy}$. This value is given in Table 1.

At 223 to 465 GHz (ALMA bands 6, 7, and 8), the extended thermal dust emission associated with a nearby spiral arm dominates, and we could only obtain upper limits on the flux density of SN 1996cr, which are also listed in Table 1.

3 MEERKAT, ATCA AND ALMA RESULTS: TOTAL FLUX DENSITIES AND SED

We show the radio light curves of SN 1996cr at 8.6 and 1.4 GHz in Figure 1. The flux density shows a steep decay since the observations of Meunier et al. (2013), who had already suggested a steepening of the decay near the end of their observations at $t \sim 6000$ d. Between the last two measurements, the flux density decays as $t^{-2.8 \pm 0.7}$ and $t^{-2.9 \pm 0.3}$ at 8.6 and 1.4 GHz, respectively.

We obtained new flux density measurements at frequencies between 1.28 and 465 GHz using MeerKAT, ATCA and ALMA (Table 1) between 2018 and 2020 ($t = 8275$ and 8911 d). We plot these flux density measurements and a fitted power-law spectral energy distribution, SED, in Figure 2. The SED shows no deviations from a power-law from 1.28 GHz up

Table 1. Total Flux Density Measurements

Freq. (GHz)	Date	Age ^a (days)	Telescope	Flux density ^b (mJy)
1.28	2018 May 4	8275	MeerKAT-16 ^c	107 ± 11
1.28	2018 Jul 20	8531	MeerKAT	99 ± 10
2.10	2020 Jan 31	8911	ATCA	60.8 ± 3.5
5.50	2020 Jan 31	..	ATCA	33.8 ± 1.9
9.00	2020 Jan 31	..	ATCA	25.1 ± 5.5
18.00	2020 Jan 31	..	ATCA	18.4 ± 1.0
34.00	2020 Jan 31	..	ATCA	12.0 ± 0.7
108.00	2019 Mar 10	8791	ALMA	4.32 ± 1.23
223.00	2019 May 5	8640	ALMA	$< 3.5^{\text{d}}$
339.90	2019 Apr 12	8617	ALMA	< 4.5
465.50	2019 Aug 6	8733	ALMA	< 22

^a The age is the time since the explosion, calculated assuming an explosion date of 1995 Sep. 7, and for the midpoint of the observations, see text §1.

^b Our standard errors include the image background rms values and a 5% flux-density calibration error, added in quadrature.

^c These observations were made using only 16 antennas, before all 64 dishes of MeerKAT became operational.

^d For the ALMA observations at $\nu > 200$ GHz, SN 1996cr was no longer distinguishable from the galaxy emission in the image, and we give as an upper limit on its flux density the typical brightness per beam of the galaxy at the location of SN 1996cr.

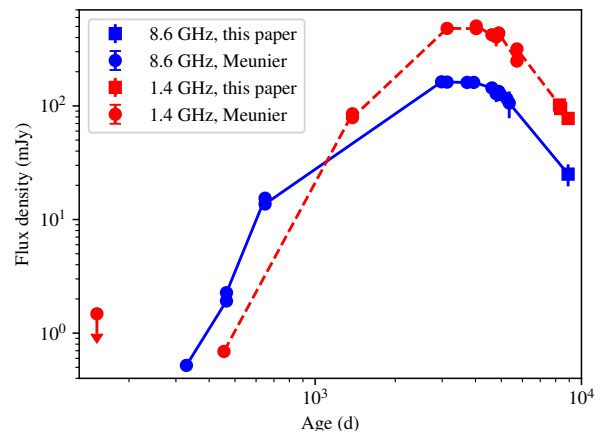


Figure 1. The radio light curves of SN 1996cr at 8.6 and 1.4 GHz, with measurements from this paper and from Meunier et al. (2013). The red points and dashed line show the 1.4 GHz light curve, while the blue points and solid line show the 8.6 GHz one. For the 1.4-GHz light curve we include values measured between 1.2 and 2.2 GHz, scaled to 1.4 GHz assuming a spectral index of -0.6 (see § 3), and for 8.4 GHz light curve we include values between 8 and 10 GHz, without any scaling.

to the highest ATCA measurement at 34 GHz, but the ALMA measurements at $\nu > 100$ GHz show that the spectrum likely steepens somewhere between 34 GHz and 223 GHz. We fit a power-law spectrum to $\nu \leq 34$ GHz using weighted least squares. Before fitting, we scaled all the measurements to a common time of 8700 d by assuming a decay $\propto t^{-2.85}$. We obtain a fitted SED of $S(\nu) = (39.8 \pm 1.0)(\nu/5 \text{ GHz})^{-0.580 \pm 0.023}$ mJy, with a $\chi^2 = 1.6$ for 5 degrees of freedom.

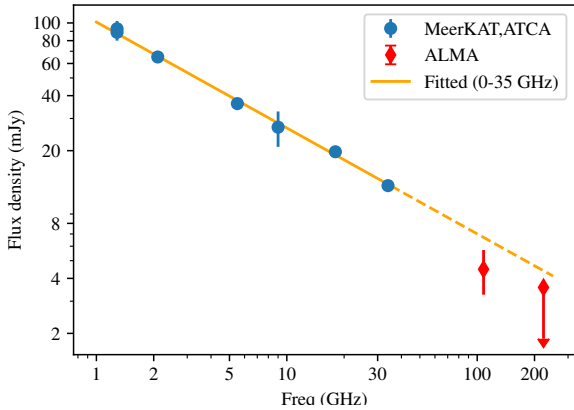


Figure 2. The radio spectral energy distribution of SN 1996cr at $t = 8700$ d (2019.5) from observations with MeerKAT, ATCA and ALMA. The orange line shows a power-law spectrum fitted by least squares for $\nu \leq 34$ GHz, which was $S(\nu) = 39.8 (\nu/5 \text{ GHz})^{-0.580}$ mJy. The flux density measurements have been scaled to a common time of $t = 8700$ d by assuming a decay rate of $S \propto t^{-2.85}$ as observed at 8.6 GHz, see § 3.

The spectral index between 34 and 108 GHz is $\alpha_{34 \text{ GHz}}^{108 \text{ GHz}} = -0.88 \pm 0.25$, and the probability that the difference in α above and below 34 GHz, and thus the apparent steepening above 35 GHz, are due to experimental error is $\sim 8\%$ ⁵. Such a steepening might be expected to occur because of synchrotron losses. However, our results are not conclusive on this point, and the degree of the steepening, as well as the corner frequency, would have to be confirmed by better high-frequency measurements.

4 VLBI OBSERVATIONS

We observed SN 1996cr using the Australian Long Baseline Array, (LBA), including the South African Hartebeesthoek antenna, at 2.3 GHz on 2020 Feb. 17 and at 4.8 GHz on 2020 March 3 (observing codes V253D and V253E, respectively). In both runs, the phased Australia Telescope Compact Array (ATCA; 5×22 m diameter used for VLBI), Ceduna (30 m), Hartebeesthoek (26 m), Hobart (26 m), Katherine (12 m), and Parkes (64 m) antennas took part, although no usable data were obtained from the Katherine antenna. At 2.3 GHz, the Tidbinbilla (DSS-36, 34 m), Warkworth AU-Scope (12 m) and Yarragadee (12 m) antennas also observed, although no usable data were obtained from either Yarragadee or Warkworth. At 4.8 GHz we also used the Warkworth 30 m and Mopra (22 m) antennas. In both cases, the observations were phase-referenced to ICRF J142455.5–680758 (PKS J1424–6807), which we will refer to as J1424–6807, and which is relatively unresolved at both frequencies.

⁵ This probability was derived numerically, the distribution of $\alpha_{34 \text{ GHz}}^{108 \text{ GHz}}$ is somewhat skew, with a tail to more negative values, so the probability of getting a value ≥ -0.580 is somewhat smaller than suggested by Gaussian statistics.

The calibration was carried out with NRAO’s Astronomical Image Processing System (AIPS; Greisen 2003). The initial flux density calibration was done through measurements of the system temperature at each telescope, and improved through self-calibration of the data from the phase-reference source J1424–6807.

For the final image, we again used the CLEAN algorithm (AIPS:imagr), and we combined the 4.8 GHz and 2.3 GHz data, so as to increase the u - v coverage. We scaled the nominal visibility amplitudes of the 2.3-GHz data by $0.8\times$ so as to match the visibility amplitude at the shortest baselines at both frequencies. Since only very partial T_{sys} measurements were available at 2.3 GHz, the flux-density scale for the 2.3-GHz data is not well known. If the absolute amplitude calibration at 2.3 GHz were better, likely the scaling between 2.3 and 4.8 GHz would be closer to the factor of 0.65 implied by the spectral index measured with ATCA and MeerKAT.

In addition to the 2020 VLBI observations described in this paper, we had obtained earlier VLBI observations of SN 1996cr with the Australian LBA, in 2007 at $t = 4307$ d and 22 GHz (observing code VX013; Bauer et al. 2008), and in 2013 at $t = 6553$ and 8.4 GHz (observing code V253C; Bietenholz 2014; Bartel & Bietenholz 2016). Both these earlier LBA observations were phase-referenced to ICRF J135546.6–632642 (PMN J1355–632), which is slightly closer on the sky than J1424–6807. ICRF J135546.6–632642 was, however significantly resolved, and thus led to problems in the phase-calibration and image reconstruction. Because of these problems, and also because of the relatively poor u - v coverage, there were significant ambiguities in the image reconstruction, and we therefore do not use the images from these epochs, but only use models fitted directly to the visibility data.

Despite the difficulties in imaging, the 2013 image (Bietenholz 2014; Bartel & Bietenholz 2016) shows a structure not dissimilar to the one from 2020 (see Fig. 3), which had much better u - v coverage and was much more reliably determined.

5 VLBI RESULTS: IMAGE

We show the VLBI image of SN 1996cr, made from the combined 2.3 and 4.8 GHz VLBI data taken in 2020, in Figure 3. The age of SN 1996cr was 8929 d for the 2.3 GHz observations, and 8959 d for the 5 GHz observations taken around a month later. Since the fractional difference in age is small, and 5-GHz data dominate, we use 8959 d as the representative age for the image. The combined 2.3 and 5 GHz observations covered a range in u - v spacing from $620 K\lambda$ to $170 M\lambda$, therefore we have some sensitivity to angular scales from 330 mas down to 1 mas .

6 VLBI RESULTS: SIZE AND EXPANSION VELOCITY

6.1 Size of the emission region

Since SN 1996cr seems to have an approximately shell-like morphology, we fit a geometrical model directly to the visibilities to determine a precise value for the angular size. The model we use is the same one used for other SNe such as

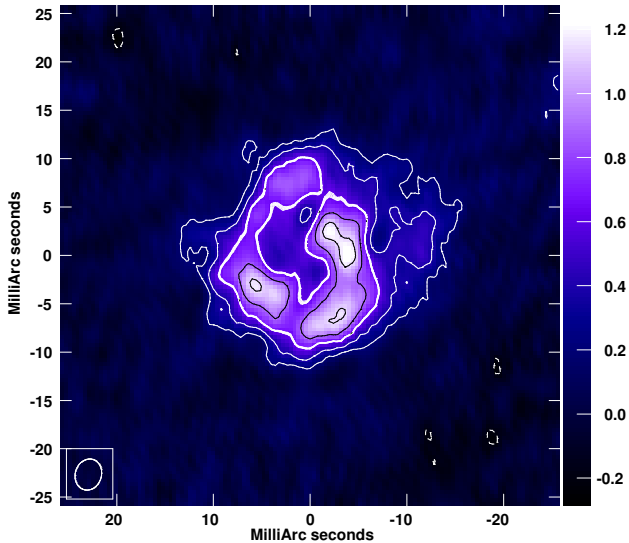


Figure 3. The VLBI image of SN 1996cr at age $t \simeq 8959$ d, made with data from the Australian Long Baseline Array, combining the data at 5 GHz, observed 2020 March 28, and the amplitude-scaled data at 2.3 GHz, observed 2020 Feb. 17, (see text for details). The restoring beam, indicated at lower left, was 3.54×2.95 mas at p.a. -15° (FWHM). With the combined data, we are sensitive to angular scales from 1 mas to 330 mas. Both the colour scale, labelled in mJy beam^{-1} , and the contours show brightness. The contours are drawn at -16 , 16 , 30 , **50** (emphasized), 70 and 90% of the peak brightness, which was $1.26 \text{ mJy beam}^{-1}$. The rms background brightness was $72 \mu\text{Jy beam}^{-1}$. North is up and east is to the left, and the origin is at the fitted position of the spherical shell model (see text, § 6.1)

SN 1993J and SN 2014C (see Bietenholz et al. 2003, 2018), and consists of the Fourier transform of the projection of an optically thin shell of emission. The model is characterized by the inner and outer angular radii of the shell, θ_i , θ_o , and the total flux density. Bietenholz et al. (2010a) showed that, in the case of SN 1993J, the results obtained through u - v plane model-fitting are superior to those obtained in the image plane. As in the imaging, we used the square root of the data weights in the fitting, which makes the results more robust at the expense of some statistical efficiency.

The outer angular radius of the model, θ_o , is most closely identified with the forward shock, and also most reliably determined by the data. Our resolution is not sufficient to reliably determine both θ_i and θ_o , and we therefore first fix the ratio $\mathcal{R}_{o/i} = \theta_o/\theta_i$ at 1.25, as this value has been shown to be appropriate in the case of SN 1993J (Bietenholz et al. 2003; Bartel et al. 2007). For the case of a simple CSM structure and a non-magnetic shell, similar values were also seen in numerical simulations (Jun & Norman 1996), although we note that the CSM structure in SN 1996cr is clearly not simple. Nonetheless, the fitted value of θ_o is only weakly dependent on the assumed value of $\mathcal{R}_{o/i}$ (with the fitted outer radius varying on the order of $\sqrt{\mathcal{R}_{o/i}}$).

Although our image (Fig. 3) was made by combining the scaled 2.3-GHz data with the 5-GHz data, it was not possible to combine the two frequencies for model-fitting. The 5-GHz

data are much more constraining, therefore we did the model-fitting only on the 5-GHz VLBI data.

Our best-fit model had an outer angular radius of $\theta_o = 9.27$ mas, with a statistical uncertainty of 0.04 mas, or $< 0.5\%$. However, as we found for SN 2014C, the statistical uncertainty is dominated by the systematic one. We follow the same procedure we used in Bietenholz et al. (2018) to estimate a systematic uncertainty, and again include three contributions in our final standard error, added in quadrature

The first contribution was estimated using jackknife re-sampling (McIntosh 2016). Specifically, we dropped the data from each of the antennas in the VLBI array in turn and calculated $N_{\text{antenna}} = 7$ new estimates (only 7 antennas contributed data to the final results) of the fitted size, and the scatter over these 7 values allows an estimate of the uncertainty of the original value that included all antennas. We obtained a jackknife uncertainty of 0.42 mas. This is much larger than the purely statistical one because the errors in the visibilities are dominated by residual calibration errors, and perhaps departures of the true morphology from the assumed model, both of which are strongly correlated from one visibility measurement to the next, rather than purely random and uncorrelated noise.

To determine the uncertainties due to the inexact-determined antenna gains, we performed a Monte-Carlo simulation by randomly adjusting the antenna gains by an rms of 10%. By subsequently refitting the size, we obtained an rms scatter of the outer angular radius of 0.45 mas. Adding these uncertainties in quadrature we obtain a final value for the fitted outer angular radius of 9.27 ± 0.60 mas. This corresponds to a linear radius of $(5.1 \pm 0.3) \times 10^{17}$ ($D/3.7 \text{ Mpc}$) cm.

Although the optically-thin spherical shell model provides a reasonable fit to the data, and a consistent way of evaluating the expansion as a function of time, the morphology in the image in Fig. 3 shows some deviations from that model. As an alternate, model-independent, means of estimating the mean radius, we turn to $\theta_{90\% \text{ flux}}$ (introduced in Bietenholz et al. 2010b), which is the mean angular radius which encloses 90% of the total flux density in the image⁶. The $\theta_{90\% \text{ flux}}$ radius is defined as the square root of the area of the relevant contour in the image divided by π . Unlike the radius, θ_o , of the model fitted directly to the visibilities, $\theta_{90\% \text{ flux}}$ is dependent to some degree on the size of the convolving beam. However, if the actual angular radius is larger than the beam, the dependence is weak.

Measuring on the image of Fig. 3, we find $\theta_{90\% \text{ flux}} = 11.9$ mas. A test shows that on a spherical shell model, convolved with our beam, $\theta_{90\% \text{ flux}}$ is $1.02 \times \theta_o$. For SN 1996cr, we find, by contrast, that $\theta_{90\% \text{ flux}}$ is 28% larger than θ_o . In other words, SN 1996cr has faint radio emission that extends beyond what is expected from a pure spherical-shell morphology. This can be seen in Fig. 3, where, particularly to the west-northwest (WNW), there is emission well beyond the bright ridge, which in a spherical shell is approximately located near the θ_i .

⁶ In Bietenholz et al. (2010b), we also used the radius of the lowest reliable contour in the image. For SN 1996cr, the lowest reliable contour was 16%, and $\theta_{90\% \text{ flux}}$ is virtually identical to the angular radius of the 16% contour in Fig. 3, so we consider only $\theta_{90\% \text{ flux}}$ in what follows.

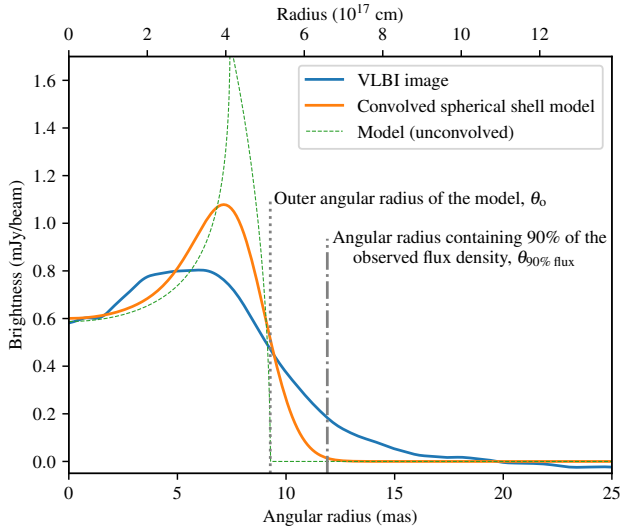


Figure 4. A radial profile of the brightness of SN 1996cr, derived from the image in Fig. 3, at age $t \simeq 8959$ d. The bottom horizontal axis shows angular radius, while the top shows linear radius (for $D = 3.7$ Mpc). The blue solid line shows the observed radial profile. The orange solid line shows the profile of the fitted optically-thin spherical model, which has $\theta_o = 9.27$ mas and $\mathcal{R}_{o/i} = 1.25$, convolved with our restoring beam (3.54×2.95 mas at p.a. -15°). The dashed green line shows the profile of the model before convolution with the restoring beam. The grey dotted and dash-dotted vertical lines show the outer angular radius of the fitted model and the observed $\theta_{90\% \text{ flux}}$ (the angular radius containing 90% of the observed total flux density), respectively.

We show a radial profile of brightness for SN 1996cr at $t = 8959$ d in Figure 4, along with the corresponding profile for the fitted model. SN 1996cr shows an excess of emission outside the fitted outer radius, θ_o , implying that a significant amount of radio emission occurs outside the model’s outer radius, thus at angular radii larger than θ_o , consequently also implying velocities higher than that derived from θ_o . The maximum in the radial profile is flatter and more extended than that in the model, suggesting that the radio emission is more spread out radially than would be expected from our shell model, which has $\mathcal{R}_{o/i} = 1.25$.

The ridge line (or locus of brightest emission) in Fig. 3 appears elliptical, with an axis ratio of $\sim 1.5:1$. If interpreted as a ring or equatorial-belt structure, rather than a complete spherical shell, this axis ratio suggests an inclination angle with respect to our line of sight, $i = 48^\circ$. This value of i is close to that of 55° estimated from the X-ray line profiles by Quirola-Vásquez et al. (2019). A CSM density distribution that was high along the minor axis direction in the image and low along the major axis one could produce such ellipticity from an initially isotropic expansion. Such a CSM density distribution is unlikely to be due to gradients in the ISM density, but could easily be created by an axisymmetric structure in either the ejecta or the CSM. This structure might be produced, for example, by a stellar wind with a polar-angle dependent flow speed or mass-loss rate. The VLBI image further suggests a possible “blow-out” region to the WNW.

We find therefore that the VLBI image suggests somewhat anisotropic expansion, which is also suggested by the X-ray

Table 2. Angular Size Estimates

Date	Age ^a (d)	θ_o (fitted shell model) ^b (mas)	$\theta_{90\% \text{ flux}}$ ^c (mas)
2020 Mar 28	8959	9.27 ± 0.60	11.9 ^a
2013 Aug 17	6554	8.21 ± 1.00^d	
2007 Jun 24	4307	5.69 ± 1.00^d	

The age is the time since the explosion, calculated to the midpoint of the observations and assuming an explosion date of 1995 Sep. 7, see text §1.

^b The outer angular radius of the fitted model of the projection of an optically thin, uniform spherical shell of emission.

^c The mean angular radius of the solid angle which encloses 90% of the total flux density in the image. Due to the unreliability of the images for 2001 and 2010 it was not possible to determine $\theta_{90\% \text{ flux}}$ for those epochs.

^d Uncertainty is estimated.

line profiles (Quirola-Vásquez et al. 2019) and the complex optical Oxygen-line emission (Bauer et al. 2008). The furthest angular extent from the fitted centre position in the VLBI image is ~ 15 mas (Figs. 3, 4), corresponding to a linear extent of $\sim 8 \times 10^{17}$ ($D/3.7$ Mpc) cm.

6.2 Expansion Velocity

As mentioned in § 4, we had also obtained earlier VLBI observations of SN 1996cr at $t = 4307$ d (2007 June 24) and 22 GHz, and again at $t = 6553$ d (2013 August 17) and 8.4 GHz (see Bauer et al. 2008; Bietenholz 2014; Bartel & Bietenholz 2016). We fitted the same spherical shell model to the visibilities of these earlier observations to obtain angular size estimates also for these two epochs. The values we obtained were $\theta_o = 5.69$ mas at $t = 4307$ d (2007) and 8.21 mas at $t = 6553$ d (2013). Uncertainties are hard to estimate since they will be dominated by the effects of the poor phase calibration, but we estimate that a value of ± 1 mas should encompass a reasonable uncertainty range. We tabulate the angular sizes in Table 2 and plot the values in Figure 5.

We fitted two expansion functions to our three values of the angular radius (Table 2) by least squares. The first function is a power-law, with

$$r(t) = (4.46 \pm 1.59) \times 10^{17} \times \left(\frac{t}{7000 \text{ d}}\right)^{(0.608 + 0.139)} \left(\frac{D}{3.7 \text{ Mpc}}\right) \text{ cm.} \quad (1)$$

The second is a constant velocity fit, with

$$r(t) = (2.9 \pm 1.3) \times 10^{17} + (4.0 \pm 0.9) \times 10^{13} \left(\frac{t - 7000}{\text{d}}\right) \left(\frac{D}{3.7 \text{ Mpc}}\right) \text{ cm,} \quad (2)$$

corresponding to a velocity of 4650 ± 1060 ($D/3.7$ Mpc) km s^{-1} . The two fitted functions are also plotted in Fig. 5. The measurements do not distinguish between these two alternate functions.

At $t = 8959$ d, the fitted outer angular radius corresponds to $(5.1 \pm 0.3) \times 10^{17} \times (D/3.7 \text{ Mpc})$ cm. This radius corresponds in turn to an average expansion since the explosion, at t_0 , of (6630 ± 430) ($D/3.7 \text{ Mpc km s}^{-1}$) (where the uncertainty includes the contribution of the ~ 200 d uncertainty in

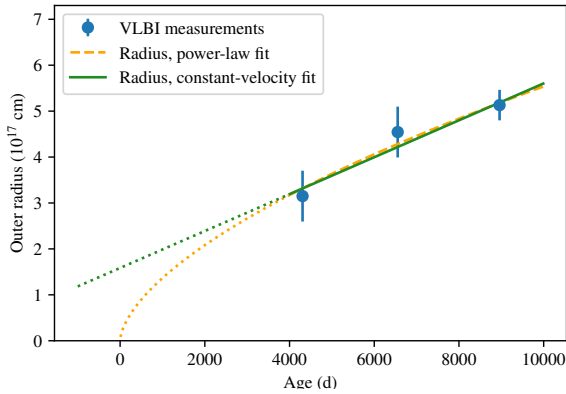


Figure 5. The angular size of SN 1996cr. We show the outer radii, θ_o , from Table 2, as determined by fitting a spherical shell model directly to the VLBI visibilities, along with their uncertainties, converted to a linear values for a distance of $D = 3.7$ Mpc. In addition, we show two fits to the outer radius values: first a power-law fit, of the form $r \propto t^m$, with $m = 0.608 \pm 0.139$ (orange dashed line), and the second a constant velocity fit of the form $r = (t - t_0) \times v$, with $v = 4650 \pm 1060$ km s $^{-1}$ (green solid line). Extrapolations beyond the range of VLBI measurements are given with respective dotted lines.

t_0). However, the radio emission extends beyond this average outer radius, particularly to the WNW, so in that direction, the mean expansion velocity since t_0 is $\sim 10^4$ km s $^{-1}$, 50% larger than the value corresponding to the outer radius of the fitted shell model.

The current velocity, estimated from our constant velocity fit between 4307 and 8959 d, is (4650 ± 1060) ($D/3.7$ Mpc) km s $^{-1}$, and is clearly lower than the average velocity since t_0 . Therefore, the expansion early on in SN 1996cr’s history must have been more rapid than it was since 4307 d.

We estimate the current velocities corresponding to $\theta_{90\% \text{ flux}}$ and to the maximum extent of the radio emission to the WNW by scaling the values obtained from θ_o and the fitted shell model, because we cannot reliably estimate those values directly from the 2007 and 2013 images. We obtain current velocities of ~ 5970 km s $^{-1}$ for $\theta_{90\% \text{ flux}}$ and 7000 km s $^{-1}$ to the WNW, both scaling as $D/3.7$ Mpc.

In summary, a representative value for the current velocity of the forward shock is (4650 ± 1060) ($D/3.7$ Mpc) km s $^{-1}$, but, judging from the extended emission to the WNW, a range of current velocities extending up to ~ 7000 ($D/3.7$ Mpc) km s $^{-1}$ seems to be present.

7 DISCUSSION

SN 1996cr, in the Circinus Galaxy, had the highest radio brightness of any spectroscopically-identified SN. We obtained new radio observations of SN 1996cr. Specifically, we obtained VLBI observations, allowing us to resolve the radio emission spatially at three epochs (4300 d to 9000 d), allowing us to infer the expansion velocity. In addition, we obtained broadband total flux density measurements at ~ 8600 d using MeerKAT, ATCA and ALMA, allowing us to monitor the evolution of the radio SED.

7.1 Spectral Index

At age $t = 8700$ d (2019.5), SN 1996cr’s SED shows an unbroken power-law down to the values measured by MeerKAT at 1.284 GHz. The synchrotron self-absorption frequency must therefore be < 1.28 GHz. Taking the average radius of 5.1×10^{17} cm (§ 6.1), and assuming the power-law spectrum with $S \propto \nu^{-0.59}$ extends down to the synchrotron self-absorption frequency, ν_{SSA} , we can calculate (Chevalier 1998) that $\nu_{\text{SSA}} = 176$ MHz, and thus well below our observations. Could we observe the SN at this frequency? The best telescope at this frequency would be the Murchison Wide-field Array (MWA), but it would not be possible to separate SN 1996cr from the Circinus Galaxy nucleus, only $\sim 23''$ away or from the diffuse emission from the galaxy.

The SED was relatively steep at $t = 397$ d but subsequently flattened with time, with α increasing at $+0.017 \pm 0.007$ year $^{-1}$ to $\alpha = -0.76$ by $t = 5370$ d (Meunier et al. 2013). Our value of $\alpha = -0.580 \pm 0.023$ at $t = 8700$ d is entirely consistent with that increase in time, despite the increase in the rate of flux density decay with time since $t = 5307$.

7.2 Radio Spectral Luminosity and its Decay

We measured a total 9-GHz flux density, $S_{9 \text{ GHz}}$, at $t = 8911$ d (2020), of 25.1 ± 5.5 mJy, corresponding to a spectral luminosity, $L_{9 \text{ GHz}}$ of $(4.1 \pm 0.9) \times 10^{26}$ ($D/3.7$ Mpc) 2 erg s $^{-1}$ Hz $^{-1}$. Few SNe have been observed at such large t , but that value of $L_{9 \text{ GHz}}$ falls within the relatively large range of values one might extrapolate for other Type IIIn SNe at $t = 8911$ d (Bietenholz et al. 2021b). In particular, SN 1996cr’s $L_{9 \text{ GHz}}$ at $t \sim 9000$ d is about twice as high as that of SN 1986J, and we note that the latter also shows a steep dropoff of radio luminosity at late times (Bietenholz & Bartel 2017).

Over the last two years, SN 1996cr’s flux density has decayed rapidly, with $S_{9 \text{ GHz}} \propto t^{-2.8 \pm 0.7}$. The two MeerKAT measurements in 2018 at 1.284 GHz give a consistent decay rate, albeit with large uncertainty, of $S_{1.3 \text{ GHz}} \propto t^{-2.6 \pm 2.3}$. In the standard, self-similar model of SN evolution, with both ejecta and CSM density profiles being power-laws in radius, there is no solution with the flux density decay as steep as this, however, steep flux density decay generally corresponds to a steep CSM density profile (see, e.g. Fransson et al. 1996). While SN 1996cr’s evolution is clearly not self-similar, the steep observed decline in the flux density may nonetheless suggest, at the present radius of $\sim 5 \times 10^{17}$ cm, a relatively steep CSM density profile, with $\rho \propto r^{-s}$ with $s > 2$, which is steeper than a wind with constant mass-loss rate and velocity, which would have $s = 2$. This picture is the opposite of what we found for SN 2014C, where the SN shock also interacted with a region of dense CSM, but we found that the CSM density outside of the dense region likely had a flat profile with $s < 2$ (Bietenholz et al. 2021a).

7.3 Morphology

Our VLBI image of SN 1996cr at $t \sim 8959$ d (Fig. 3) shows a morphology resembling that of an optically-thin spherical shell seen in projection. Such a morphology is similar to that of the other SNe that have so far been reliably resolved (Bietenholz 2014; Bartel et al. 2017; for example, see e.g. Bi-

et al. 2003; Marcaide et al. 1995 on SN 1993J). A shell-like morphology is also expected on theoretical grounds (e.g. Chevalier & Fransson 2017).

However, SN 1996cr shows notable departures from a circularly symmetric morphology on the sky. The ridge line, or locus of brightest emission, appears to be somewhat elliptical, and emission of lower surface brightness extends well beyond the ridge-line, especially to the WNW. The elliptical ridge-line suggests a circular structure tilted to the plane of the sky by $\sim 48^\circ$.

Quirola-Vásquez et al. (2019) found that the X-ray line profiles also suggested complex morphology for SN 1996cr, with neither a spherical shell nor a simple ring-like geometry being compatible with the observed profiles. In particular, Quirola-Vásquez et al. (2019) suggested that there are two X-ray emitting components: a lower-temperature one with $T \simeq 2$ keV with a wide angle of outflow, and one with a higher $T \simeq 20$ keV and a narrower angle of outflow. They associate the hotter, narrow-angle outflow with a reflected shock, formed when the ejecta impacted on the dense CSM region, currently propagating inward (in a co-moving frame) into the already shocked CSM interior to the forward shock, further heating this material and thus producing the high temperatures.

7.4 Expansion Velocity

We determined the expansion velocity of SN 1996cr by tracking the evolution of the radius between our three VLBI epochs. We obtained mean radii of SN 1996cr by fitting an optically-thin spherical shell model, which can account for the bulk of the emission, to our VLBI data, and we took the outer radius of this fitted model to be a representative mean value for the radio emission region and location of the forward shock. At $t = 8859$ d, this value was $(5.1 \pm 0.4) \times 10^{17}$ ($D/3.7$ Mpc) cm, corresponding to a mean velocity since the explosion of (6700 ± 430) ($D/3.7$ Mpc) km s^{-1} . This velocity is comparable to, albeit slightly lower than that seen for other Type II SNe at similar ages: for example, SN 1993J had a mean velocity of $11,300 \text{ km s}^{-1}$ at $t = 3164$ d (Bartel et al. 2002), which, extrapolating the deceleration, would equal 9700 km s^{-1} at $t = 8959$ d; while SN 1986J had one of 8790 km s^{-1} at $t = 8333$ d (Bietenholz et al. 2010b).

By using also the radii determined from our VLBI measurements from 2007 and 2013, we found that the present expansion velocity of SN 1996cr, again as determined from the fitted spherical shell model, was roughly constant at (4650 ± 1060) ($D/3.7$ Mpc) km s^{-1} over the period $4307 \leq t \leq 8859$ d.

Our measurements clearly show that the forward shock has been decelerated since the explosion: the explosion date around 1995 Sep. (see, e.g. Bauer et al. 2008) requires that the velocity before our first VLBI measurement at $t < 4307$ d must have been higher at $\gtrsim 11,000 \text{ km s}^{-1}$ (Fig. 5).

Quirola-Vásquez et al. (2019) determined velocities from the X-ray line profiles, and at $t \simeq 4900$ d, found maximum velocities of $\sim 5000 \text{ km s}^{-1}$ for elements such as Si, but only $\sim 3000 \text{ km s}^{-1}$ for Fe at $t \simeq 4900$ d. The velocities seen in the X-ray, being lower than those seen in the radio, are consistent with the expectation that the X-ray emission arises near the reverse shock, or near a reflected shock, formed when the

forward shock first encountered the dense CSM at $t \sim 500$ d, since the reverse and reflected shocks are generally expected to have a lower velocity than the forward one.

There is a wealth of evidence that the expanding shock in SN 1996cr first moved rapidly through a relatively low density medium immediately surrounding the progenitor, before impacting on dense CSM at radius $\sim 10^{17}$ cm at around $t \sim 500$ d after the explosion (Bauer et al. 2008; Dwarkadas et al. 2010; Meunier et al. 2013; Quirola-Vásquez et al. 2019). Our earliest VLBI measurement at $t = 4307$ d, however, was considerably later than this impact. Indeed, in the simulations of Dwarkadas et al. (2010), the forward shock impacts on a shell of dense CSM shell, then passes through and exits the shell again at $t \sim 2500$ d, all before the first VLBI measurement. In those simulations the shock velocity remains approximately constant at $v \sim 4650 \text{ km s}^{-1}$ after $t \sim 3000$ d. This behaviour corresponds well to the VLBI measurements of the expansion.

The shock is thought to have impacted on the dense CSM at around $t \sim 500$ d. Extrapolating our constant-velocity fits to the expansion curve back towards that time, we obtain a radius of $(1.8 \pm 0.6) \times 10^{17}$ ($D/3.7$ Mpc) cm. The VLBI measurements therefore suggest an outer radius of $\sim 1.8 \times 10^{17}$ cm at the time of the impact of the shock on the dense CSM. This value is somewhat larger than has been used in the modelling, e.g. 10^{17} cm in Dwarkadas et al. (2010) and Dewey et al. (2011), suggesting a more rapid expansion before the impact on the dense CSM.

Given that the VLBI image (Fig. 3) shows some significant departures from a spherical-shell morphology, a range of expansion velocities for the forward shock will be present at any one time. In particular the radio emission beyond the boundary of the fitted spherical shell suggests expansion velocities, for $4307 \leq t \leq 8859$ d, of up to $\sim 7000 \text{ km s}^{-1}$ to the WNW (see § 6.2).

Although the limited dynamic range and resolution of the VLBI image do not allow a conclusive determination of the three-dimensional source structure, the morphology could perhaps be interpreted in terms of a ring or equatorial-band-like radio-bright region, tilted to the line of sight. This radio-bright region is likely produced by a similarly-shaped region of higher density in the CSM.

There appears to be some similarity between the radio morphology of SN 1987A and SN 1996cr. We may therefore go a step further and assume that there is a similarity in their formation mechanisms. In SN 1987A, the brighter radio emission is caused by the interaction of the shock with the narrow waist of an hourglass or peanut-shaped cavity in an HII region into which the SN expands, which results in an equatorial-belt like region of denser CSM and consequently brighter radio emission (Orlando et al. 2019). Note that in SN 1987A's case there is also a set of three rings of even higher density, however, these are not thought to affect the radio brightness greatly. The progenitor of SN 1987A is presumed to have had a binary companion, and it is thought that binary interaction shaped the cavity in the HII region (and also the dense rings; see e.g. Potter et al. 2014; Orlando et al. 2015, 2019).

We may then postulate, on the basis of the morphological similarity, that SN 1996cr's progenitor star also had a companion, and that binary interaction was also the cause of the global asymmetry. SN 1996cr's progenitor was constrained to be a W-R or BSG star by Dwarkadas et al. (2010). Sim-

ilar to the scenario in SN 1987A, it is the interaction of the wind from the progenitor immediately prior to the explosion, that is when the progenitor was in the W-R or BSG epoch of its evolution, with that from a previous, likely RSG epoch, that leads to the formation of a wind bubble around the star. Asymmetries in the RSG wind would then lead to a global asymmetry in CSM structure, which would be reflected in the radio and X-ray profiles of the SN. Note that simulations have shown that there are considerable instabilities in the wind-blown bubbles around massive stars, which lead strong departures from spherical symmetry for the CSM (see, e.g. Dwarkadas 2022), although such instabilities are more likely to produce a clumpy structure than the global asymmetries seen in the radio emission. Such instabilities may, however, enhance any global asymmetries present in the wind.

The forward shock is slowed significantly where it impacts on the denser CSM, but continues to expand more rapidly along the directions where the CSM is less dense. In SN 1996cr’s case, the forward shock encountered the dense CSM first at $t \sim 500$ d at a radius of $\sim 1.8 \times 10^{17}$ cm (as opposed to $\sim 3 \times 10^{17}$ cm for SN 1987A). In this picture, that denser CSM would be a ring or equatorial belt, perhaps the narrow waist of an hourglass- or peanut-shaped cavity (as in SN 1987A). The interaction would then produce the tilted-ring morphology of the ridge-line in the VLBI image. Other portions of the forward shock, however, moving along the axial direction, would continue moving more rapidly. It seems also that some departures from cylindrical symmetry are required to explain the asymmetry in the VLBI image, which has more extended emission to the WNW than to the ESE. Such an asymmetrical “blowout” is seen in the supernova remnant SNR G0.9+0.1 where the outflow is likely due to the pulsar embedded in the nebula, but is considerably more pronounced on one side than the other (Heywood et al. 2022). Such an asymmetry could perhaps also explain the asymmetries seen in the X-ray line profiles.

8 CONCLUSIONS AND SUMMARY

We obtained VLBI observations of SN 1996cr, and for the first time reliably imaged the radio emission. We have also obtained total flux density observations allowing us to monitor the evolution of the radio spectral energy distribution. SN 1996cr is thought to have exploded in a low-density region, but then the shock interacted with a massive shell in the CSM after $t = 1 \sim 2$ yr. We found the following:

1. Our new VLBI observations show a structure which is relatively circular in outline. Within this outline, the brightest emission is somewhat elliptical, but generally near the outside edge (edge-brightened), except on WNW, where fainter emission extends well beyond the bright ridge-line. The morphology in the VLBI image is approximately consistent with the projection of a spherical shell, but the slight ellipticity of the ridge-line may suggest instead a circular structure, tilted to the plane of the sky.
2. At $t = 8859$ d, the average outer radius of the radio emission, likely close to that of the forward shock, is $(5.1 \pm 0.3) \times 10^{17}$ ($D/3.7$ Mpc) cm, as determined by fitting a spherical shell model to the radio emission.
3. The average expansion velocity since the explosion, again determined from the fitted spherical shell, is $6630 \pm$

430 ($D/3.7$ Mpc) km s^{-1} . The average expansion velocity over the time of the three VLBI measurements ($4307 \leq t \leq 8959$ d, or 2007 to 2020) was (4650 ± 1060) ($D/3.7$ Mpc) km s^{-1} . This difference implies that the expansion had been significantly decelerated already before our first VLBI measurement at $t = 4307$ d. Although our data do not allow us to say whether this deceleration is ongoing, or whether it occurred mostly before $t = 4307$ d, the physical picture of the shock impacting on a dense CSM shell at $t \sim 500$ d suggests the latter.

4. The deviations of the observed radio morphology from that of a projected spherical shell suggest the presence of a range of expansion velocities for the forward shock, in particular, with some segments expanding at up to ~ 7000 km s^{-1} during $4307 \leq t \leq 8959$ d. The range of velocities seen in X-ray line profiles is a bit lower, consistent with the expectation that the X-ray emission comes from the reverse or reflected shocks interior to the forward one.

5. If we assume an approximately constant velocity expansion since $t \sim 500$ d, then the VLBI measurements suggest a radius at that time of $(1.8 \pm 0.6) \times 10^{17}$ ($D/3.7$ Mpc) cm. This radius therefore corresponds to the inner radius of the dense CSM region, and is somewhat larger than the $\sim 1 \times 10^{17}$ cm that has been assumed in the hydrodynamic models so far, suggesting higher initial expansion velocities and a stronger deceleration upon interacting with the dense CSM shell, or an asymmetry in the ejecta/shell, or perhaps an incomplete shell.

6. SN 1996cr’s radio flux density has decreased rapidly since 2006, proportional to $t^{-2.9}$. This could be due to a steep CSM density profile, with $s > 2$ where $\rho \propto r^{-s}$.

7. The spectral index of the radio emission between 1 and 34 GHz at $t = 8700$ d (2019.5), was $\alpha = -0.580 \pm 0.023$ with the spectrum over that range well described by a power-law. The spectrum likely steepens above 35 GHz.

8. The spectrum below 35 GHz, which we found had $\alpha = -0.580 \pm 0.023$ at $t = 8700$ d, has continued to flatten with time since the value of $\alpha = -0.76$ reported at $t = 5370$ d by Meunier et al. (2013).

ACKNOWLEDGEMENTS

We thank Tony Foley (1957 to 2021) for carrying out the observations of SN 1996cr with MeerKAT. We thank the teams of the LBA, MeerKAT and ATCA for their work to make the observations possible. The Australia Telescope Compact Array is part of the Australia Telescope National Facility (<https://ror.org/05qajvd42>) which is funded by the Australian Government for operation as a National Facility managed by CSIRO. We acknowledge the Gomeri people as the traditional owners of the ATCA Observatory site. the South African Radio Astronomy Observatory, a facility of the National Research Foundation, an agency of the Department of Science and Innovation. This paper makes use of the following ALMA data: ADS/JAO.ALMA#2018.1.00007.S. ALMA is a partnership of ESO (representing its member states), NSF (USA) and NINS (Japan), together with NRC (Canada), MOST and ASIAA (Taiwan), and KASI (Republic of Korea), in cooperation with the Republic of Chile. The Joint ALMA Observatory is operated by ESO, AUI/NRAO and NAOJ. This research has made use of the NASA/IPAC Extragalac-

tic Database (NED), which is funded by the National Aeronautics and Space Administration and operated by the California Institute of Technology. We have made use of NASA's Astrophysics Data System Abstract Service. This research was supported by both the National Sciences and Engineering Research Council of Canada and the National Research Foundation of South Africa. Additional funding for FEB was provided by ANID - Millennium Science Initiative Program - ICN12_009, CATA-Basal - FB210003 (FEB), and FONDECYT Regular - 1190818 and 1200495. VVD is supported by NSF grant AST-1911061.

DATA AVAILABILITY STATEMENT

The raw data underlying this paper are available in the Australian Telescope National Facility archive, <http://atoa.atnf.csiro.au>, the South African Radio Astronomy Observatory archive <https://archive.sarao.ac.za>, and the ALMA archive <https://almascience.nrao.edu/aq>. Other data will be shared on reasonable request.

REFERENCES

- Bartel N., Bietenholz M. F., 2016, in *Supernova Remnants: An Odyssey in Space after Stellar Death*. p. 133
- Bartel N., et al., 2002, *ApJ*, **581**, 404
- Bartel N., Bietenholz M. F., Rupen M. P., Dwarkadas V. V., 2007, *ApJ*, **668**, 924
- Bartel N., Karimi B., Bietenholz M. F., 2017, *Astronomy Reports*, **61**, 299
- Bauer F., 2007, *Central Bureau Electronic Telegrams*, **876**, 14
- Bauer F. E., Brandt W. N., Sambruna R. M., Chartas G., Garmire G. P., Kaspi S., Netzer H., 2001, *AJ*, **122**, 182
- Bauer F. E., Dwarkadas V. V., Brandt W. N., Immler S., Smartt S., Bartel N., Bietenholz M. F., 2008, *ApJ*, **688**, 1210
- Bietenholz M., 2014, in Tarchi A., Giroletti M., Feretti L., eds, *12th European VLBI Network Symposium and Users Meeting (2014)*, published by SISSA, Trieste. p. 51
- Bietenholz M. F., Bartel N., 2017, *ApJ*, **851**, 7
- Bietenholz M. F., Bartel N., Rupen M. P., 2003, *ApJ*, **597**, 374
- Bietenholz M., et al., 2010a, in *10th European VLBI Network Symposium and EVN Users Meeting: VLBI and the New Generation of Radio Arrays*. ([arXiv:1103.1783](https://arxiv.org/abs/1103.1783))
- Bietenholz M. F., Bartel N., Rupen M. P., 2010b, *ApJ*, **712**, 1057
- Bietenholz M. F., Kamble A., Margutti R., Milisavljevic D., Soderberg A., 2018, *MNRAS*, **475**, 1756
- Bietenholz M. F., Bartel N., Kamble A., Margutti R., Matthews D. J., Milisavljevic D., 2021a, *MNRAS*, **502**, 1694
- Bietenholz M. F., Bartel N., Argo M., Dua R., Ryder S., Soderberg A., 2021b, *ApJ*, **908**, 75
- CASA Team et al., 2022, *PASP*, **134**, 114501
- Chevalier R. A., 1998, *ApJ*, **499**, 810
- Chevalier R. A., Fransson C., 2017, *Thermal and Non-thermal Emission from Circumstellar Interaction*. p. 875
- Dewey D., Bauer F. E., Dwarkadas V. V., 2011, in McEnery J. E., Racusin J. L., Gehrels N., eds, *American Institute of Physics Conference Series Vol. 1358*, American Institute of Physics Conference Series. pp 289–292 ([arXiv:1102.1442](https://arxiv.org/abs/1102.1442)), [doi:10.1063/1.3621791](https://doi.org/10.1063/1.3621791)
- Drissen L. N., et al., 2022, *MNRAS*, **512**, 5037
- Dwarkadas V. V., 2022, *Galaxies*, **10**, 37
- Dwarkadas V. V., Gruszko J., 2012, *MNRAS*, **419**, 1515
- Dwarkadas V. V., Dewey D., Bauer F., 2010, *MNRAS*, **407**, 812
- Francis L., Johnstone D., Herczeg G., Hunter T. R., Harsono D., 2020, *AJ*, **160**, 270
- Fransson C., Lundqvist P., Chevalier R. A., 1996, *ApJ*, **461**, 993
- Fransson C., et al., 2014, *ApJ*, **797**, 118
- Freeman K. C., Karlsson B., Lynga G., Burrell J. F., van Woerden H., Goss W. M., Mebold U., 1977, *A&A*, **55**, 445
- Greisen E. W., 2003, in Heck A., ed., *Astrophysics and Space Science Library*, Berlin Springer Verlag Vol. 285, *Information Handling in Astronomy - Historical Vistas*. p. 109, [doi:10.1007/0-306-48080-8-7](https://doi.org/10.1007/0-306-48080-8-7)
- Heywood I., 2020, *oxkat: Semi-automated imaging of MeerKAT observations* ([ascl:2009.003](https://ascl.net/2009.003))
- Heywood I., et al., 2022, *ApJ*, **925**, 165
- Jun B., Norman M. L., 1996, *ApJ*, **465**, 800
- Marcaide J. M., et al., 1995, *Science*, **270**, 1475
- McIntosh A., 2016, preprint ([arXiv:1606.00497](https://arxiv.org/abs/1606.00497))
- Meunier C., et al., 2013, *MNRAS*, **431**, 2453
- Milisavljevic D., et al., 2015, *ApJ*, **815**, 120
- Mondal S., Róžańska A., Bagińska P., Markowitz A., De Marco B., 2021, *A&A*, **651**, A54
- Orlando S., Miceli M., Pumo M. L., Bocchino F., 2015, *ApJ*, **810**, 168
- Orlando S., et al., 2019, *A&A*, **622**, A73
- Partridge B., López-Caniego M., Perley R. A., Stevens J., Butler B. J., Rocha G., Walter B., Zacchei A., 2016, *ApJ*, **821**, 61
- Planck Collaboration et al., 2020, *A&A*, **641**, A6
- Potter T. M., Staveley-Smith L., Reville B., Ng C. Y., Bicknell G. V., Sutherland R. S., Wagner A. Y., 2014, *ApJ*, **794**, 174
- Quirola-Vásquez J., Bauer F. E., Dwarkadas V. V., Badenes C., Brandt W. N., Nymark T., Walton D., 2019, *MNRAS*, **490**, 4536
- Ransome C. L., Habbergham-Mawson S. M., Darnley M. J., James P. A., Filippenko A. V., Schlegel E. M., 2021, *MNRAS*, **506**, 4715
- Róžańska A., Bresler K., Beldycki B., Madej J., Adhikari T. P., 2018, *A&A*, **612**, L12
- Sambruna R. M., Brandt W. N., Chartas G., Netzer H., Kaspi S., Garmire G. P., Nousek J. A., Weaver K. A., 2001, *ApJ*, **546**, L9
- Smith N., 2014, *ARA&A*, **52**, 487